Journal of Neuroinflammation

RESEARCH

Open Access

# Sex chromosomes and gonads modify microglial-mediated pathology in a mouse model of Alzheimer's disease

Brad T. Casali[1], Li Lin[1], Olesia Benedict[1], Hannah Zuppe[1], Emily Marsico[1] and Erin G. Reed[1*]

**Abstract**

Alzheimer's disease (AD) is a neurodegenerative disorder disproportionally affecting women with sex-specific disease manifestations and therapeutic responses. Microglial-mediated inflammation occurs in response to and perpetuates disease processes, and fundamental sex differences in microglia may contribute to these sex biases. Both sex chromosomes and gonad-derived hormones shape immune responses, but their contribution to immune-mediated mechanisms underlying the sex bias in AD is unclear. Crossing the Four Core Genotype (FCG) model to separate sex chromosome and gonad-derived hormone effects to the 5xFAD model, we found the sex chromosome complement impacted microgliosis, neuroinflammation, plaque burden and neuritic dystrophy. Modification of pathology largely correlated with microgliosis, and sex chromosomes and gonad-derived hormones influenced plaque remodeling and microglial CD11c expression. Our results provide potential trajectories for studying and targeting microglial-mediated sex differences and emphasize the complex interplay between sex chromosomes and hormones during AD.

**Keywords** Microglia, Alzheimer's disease, Plaque, Inflammation, 5xFAD, Sex differences, Plaque, Gonads, Hormones

## Background

Alzheimer's disease (AD) is a neurodegenerative disease resulting in cognitive decline due to accumulating extracellular β-amyloid (Aβ) plaques, intracellular aberrantly hyperphosphorylated tau, dysregulated neuroinflammation and neuronal death. AD and other dementias affect approximately 7 million Americans aged 65 years or older [1], with nearly 4 million being women. Additionally, men and women experience different clinical trajectories [5].

A variety of causes contribute to these sexually dimorphic effects, including sex-related factors such as sex chromosomes and circulating gonadal hormones (reviewed in [37]). Microglia, the innate immune cells of the brain, exhibit sex-specific phenotypes and gene expression profiles across the lifetime [7, 21, 40], which may underlie sex-specific responses in the context of neurodegenerative diseases [33]. The X chromosome contains a significant number of genes and microRNAs with immunoregulatory functions [6, 38]. Gonad-derived sex hormones orchestrate neonatal brain patterning, circuitry and microglial responses. Furthermore, sexually dimorphic microglial phenotypes may be evoked later in adulthood by sex-specific hormones [40]. Both sex chromosomes and hormones direct immune responses in sexually dimorphic ways [34]. It is unclear whether sex chromosomes and/or gonadally derived hormones differentially contribute to AD-related microglial phenotypes, pathology and progression.

Since gonad-derived hormones can interact with gene products encoded from sex chromosomes, we leveraged the Four Core Genotypes (FCG) mouse model to decouple sex chromosomes and gonads [2]. We crossed

*Correspondence:
Erin G. Reed
ereedgeaghan@neomed.edu
[1] Department of Pharmaceutical Sciences, Northeast Ohio Medical University, 4209 St. Rt. 44, Rootstown, OH 44272, USA

FCG mice to the 5xFAD mouse model to examine the impacts of sex chromosomes and intact gonads on AD progression and pathology. Depending on gonads and age, we observed the presence of a second X chromosome strongly enhanced microgliosis and microglial numbers, plaque burden and neuritic dystrophy, whereas the Y chromosome exhibited a blunted effect. Both neuron retention, microglial neurodegenerative phenotypes and microglial gene expression were similarly regulated by sex chromosomes depending on gonads. Our findings highlight the complexity of sex chromosomes and circulating hormones in regulating neuroinflammatory phenotypes in AD pathology.

## Materials and methods

### Transgenic animal models and experimental paradigm

Four-Core Genotype (FCG) mice were purchased from The Jackson Laboratory (Strain #010905 and originally described in [2]. These mice carry a transgene of mutation in the testes-determining portion of the *Sry* gene on the Y chromosome ($Y^{-Sry}$)—this transgene is translocated to chromosome 3, resulting in offspring which may carry the *Sry* transgene, but may possess either testes ($XY^{-Sry}$ and XX*Sry*) or ovaries (XX and $XY^{-Sry}$). The 5xFAD mouse model (B6.Cg-Tg(APPSwFlLon,PSEN1*M 146L*L286V)6799Vas/Mmjax, RRID:MMRRC_034848-JAX) was obtained from the Mutant Mouse Resource and Research Center (MMRRC) at the Jackson Laboratory, an NIH-funded strain repository, and was donated to the MMRRC by Robert Vassar, PhD., Northwestern University. The 5xFAD strain was originally described [31]. To generate experimental crosses, $XY^{-Sry}$ testes-bearing FCG mice were crossed to 5xFAD-transgenic female mice, and offspring were aged to either 4-or 8-months old (see Fig. 1A. Color-coded bars correspond to each timepoint in the graphs: red and blue bars represent 4 months and purple, and green represent 8 months for 5xFAD; FCG groups. All animals had access to food and water ad libitum and were on a 12-h light/dark cycle. All animal procedures were approved by the Institutional Animal Care and Use Committee at NEOMED.

### Isolation, processing and homogenization of brain samples

Animals were deeply anesthetized with isoflurane using a vaporizer and then euthanized via cervical dislocation. Whole blood was collected, and the brain was bisected. One brain hemisphere was dropped-fixed in 4% paraformaldehyde overnight at 4 °C. The cortex was dissected on ice from the remaining hemisphere and samples were stored on dry ice and held at −80 °C until homogenization. Tissue was homogenized using a rotor–stator homogenizer in ice-cold tissue homogenization buffer (1 M Tris, 8.5% sucrose [w/v], 0.5 M EDTA and 0.2 M EGTA in ultrapure water, pH 7.4) supplemented with fresh protease inhibitor cocktail (Sigma #P3480; 1:100 dilution).

### Immunohistochemistry

Brains were dehydrated in 30% sucrose in PBS at 4 °C until they sank. Brains were then embedded and sectioned as sagittal 30 µm sections into storage cryoprotectant (30% glycerol, 30% ethylene glycol in PBS) on a cryostat (Leica). At least two anatomically matched brain sections from individual animals were washed in 0.1% PBS-Triton-X (PBST) and retrieved for 10 min. at 95 °C in either Reveal Decloaker, RTU (Biocare Medical RV1000MMRTU) or 10 mM sodium citrate, pH 6.0, depending on the staining combination. For 6E10, GFAP and IBA1 staining, sodium citrate was used as the retrieval solution; the remaining staining combinations used 1X Decloaker. After retrieval, sections were cooled, blocked for 1 h. at room temperature (RT) in blocking solution (5% normal-donkey serum, 0.3% Triton-X in PBS) and stained overnight with primary antibody in blocking solution at 4 °C. The following antibodies were used at 1:1000 dilution unless otherwise stated: mouse MOAB-2 (Novus Biologicals #NBP2-13075); mouse 6E10 (β-amyloid, 1–16, BioLegend #803004); rat GFAP (ThermoFisher Scientific #13-0300); rabbit CD68 (Cell

(See figure on next page.)

**Fig. 1** Sex chromosomes and gonads modify cortical plaque burden and neuroinflammation in 4-month-old 5xFAD; FCG mice. **A** 5xFAD; FCG experimental paradigm. XY- Sry (FCG) mice were mated to 5xFAD mice to generate experimental 5xFAD; FCG mice, producing the following: XY- Sry (XY- testes; XY-T), XX Sry (XX testes; XXT), XX (XX ovaries; XXO) and XY- (XY- ovaries; XY-O) mice. Wildtype FCG littermates were also generated, and mice were aged to 4- and 8-months old. **B** Representative cortical images for GFAP (blue), IBA1 (green) and 6E10 (red). **C** *i*, percent 6E10 cortical plaque coverage; *ii*, number of 6E10 + cortical plaque species. **D** *i*, fold change cortical Aβ protein expression; *ii*, fold change cortical APP C-terminal fragment (CTF) protein expression. **E** Percent GFAP cortical coverage. **F** Percent IBA1 cortical coverage. **G** Number of IBA1 + cortical cells. **H** Representative cortical MOAB-2 staining (green). *i*, average number of MOAB 2 cortical plaques. *ii*, percent MOAB-2 cortical coverage. **I** Images of cortical IBA1 (green), 6E10 (red) and CD68 (blue) with percent CD68 (**J**), percent double positive CD68/6E10 normalized to 6E10 area (**K**) and average #IBA1 + cell per plaque (**L**). **M**–**R** Fold changes relative to wildtype FCG animals of indicated mRNA cortical genes in 5xFAD; FCG animals. **M** *Iba1*, **N** *Trem2*, **O** *Gfap*, **P** *Il1b*, **Q** *Apoe* and **R** *Tnfa*. Two-way ANOVA with Tukey post-hoc correction significance indicated by brackets; ns = not significant. N ≥ 3 mice per group. Scale bars for images are 50 µm

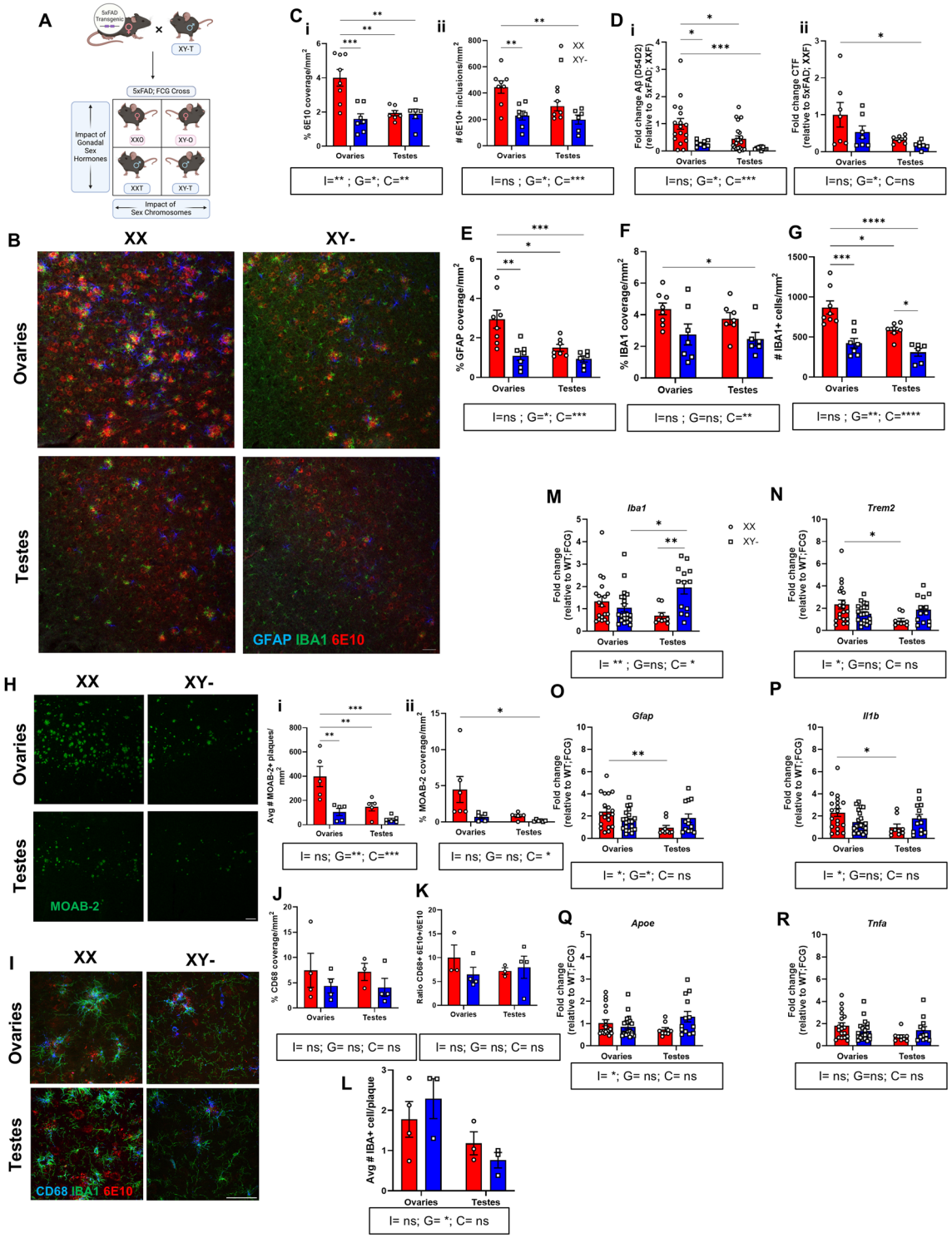


**Fig. 1** (See legend on previous page.)

Signaling Technology, clone E3O7V), #97778), rabbit IBA1 (WAKO #019-19741); rat LAMP-1 (DSHB, #1D4B; 1:2000); rabbit ubiquitin (ThermoFisher Scientific #PA1-10023; 1:2000); mouse Nt-APP (Millipore Sigma, MAB348, used at 1:2000); guinea pig NeuN (Synaptic Systems #266-004); and rabbit CD11c (Cell Signaling Technology, clone D1V9Y, #97585; 1:500). Sections were washed three times in PBST and incubated in the

appropriate secondary-conjugated antibodies for 1 h. at RT: donkey anti-guinea pig IgG Alexa Fluor 488 (Jackson ImmunoResearch Laboratories, # 706-545-148); donkey anti-rat IgG Alexa Fluor 488 (ThermoFisher Scientific Cat # A-21208); donkey anti-rabbit IgG Alexa Fluor 546 (ThermoFisher Scientific Cat # A10040); donkey anti-mouse IgG Alexa Fluor 647 (ThermoFisher Scientific Cat # A-31571); or donkey anti-rabbit IgG Alexa Fluor 647 (ThermoFisher Scientific Cat #A-31573). In some instances, sections were then washed and mounted. For X34 staining (Sigma #SML1954), sections were washed after secondary antibody and mounted onto slides and dried for at least 1 h. at RT. Slides were immersed in PBS for 5 min. and incubated for 10 min. in working X34 solution (10 μM in 40% ethanol/0.02 N NaOH/PBS), washed for 5 min. in PBS, coverslipped in ProLong Gold (ThermoFisher Scientific #P36930), air-dried and then imaged.

#### Image acquisition

The following staining panels were acquired on a Leica confocal (TCS SPE DMI8) microscope: 6E10, GFAP and IBA1; X-34, Lamp-1, Ubiquitin and Nt-APP; and CD68, IBA1 and 6E10. Images were acquired using a system-optimized Z-stack with either an air 10X objective (NA = 0.3, zoom factor of 1 and pinhole of 1.0 AU for 6E10/GFAP/IBA1) or an oil-immersed 20X objective (for dystrophy staining, NA = 1.15, zoom factor of 1.0 and pinhole of 1.0 AU; for CD68/IBA1/6E10, NA = 1.15, zoom factor of 1.5 and pinhole of 1.0 AU). NeuN staining and plaque compaction using 6E10 and X34 staining were acquired using an upright, epifluorescent microscope M2 (Zeiss). MOAB2 and CD11c images were acquired on the upright, epifluorescent microscope AxioZoom V16 (Zeiss). All image acquisition was performed using similar gain and exposure settings.

#### Image analysis and image quantification

All image processing and analysis was performed using FIJI (NIH). For simplicity, all confocal Z-stack images for specimens were collapsed into a single z-plane using a maximum projection via FIJI. Images were manually threshold and the percentage of immunoreactive area quantified. In graphs, the quantified stains are represented as percent coverage normalized to areas of interest. For microglial, 6E10 and NeuN counts, manual thresholds were applied to areas of interest and objects were separated using the "watershed" function followed by "analyze objects" with 2 $um^2$ cutoff and objects excluded from edges of the image. For X-34 plaque compaction, circularity cutoffs were as follows: filamentous 0–0.14; intermediate, 0.15–0.28; and compact > 30 [10]. For 6E10 +, X34 + and 6E10 + /X34 + analysis, individual plaque types were manually counted. Intraneuronal 6E10 + staining was not counted in these analyses. For CD68 and 6E10 overlap, both stains were manually threshold, masks were created for each stain and the area covered by both CD68 and 6E10 stains was measured using Fiji. This measurement is represented as ratio of both CD68 + 6E10 + normalized to total 6E10 area. Plaques within the field of view were selected and microglial were manually counted and normalized to plaque number. Plaque sizes were binned into specific size ranges using Excel (Microsoft) histogram function. Images were analyzed and quantified by observers blinded to genotypes.

#### Quantitative, reverse-transcription polymerase chain reaction (qPCR)

Immediately following tissue homogenization, an aliquot of homogenate was combined 1:1 with RNASTAT (Amsbio, #CS-111), vortexed and placed on dry ice until RNA extraction. RNA was extracted using PureLink RNA Mini Kit columns (ThermoFisher Scientific #12183025) following manufacturer's recommendations, but with slight modifications. Briefly, chloroform was combined with RNASTAT, the aqueous phase was extracted and then applied to RNA Mini columns. The manufacturer's suggested recommendations were then followed, and contaminating genomic DNA was eliminated using the PureLink DNase Set (ThermoFisher Scientific #1285010) on the RNA column. RNA was eluted, measured and reverse-transcribed into cDNA using High-Capacity cDNA Reverse Transcription Kit (ThermoFisher Scientific #4368814) following the manufacturer's instructions. Gene expression was measured using Taqman Probe Assays and Taqman Master Mix following manufacturer's instructions using QuantStudio Flex 6 (Applied Biosystems). Relative mRNA expression was normalized to housekeeping genes *18S* and *Gapdh* for all probes. Wildtype FCG results are displayed as fold-change relative to XXF, while 5xFAD; FCG results are displayed as fold-change relative to the corresponding wildtype FCG genotype.

#### Protein analysis

Tissue homogenates were clarified, and protein concentration was measured using the BCA method. Protein expression was analyzed via immunoblotting using the JESS capillary Western blotting method (Protein Simple), following manufacturer's suggested protocol. Primary antibodies, dilutions and diluents used were as follows: Aβ (clone D54D2, Cell Signaling Technology # 8243; 1:2000; Diluent 2); PSD95 (Abcam, #ab2723; 1:200; Diluent 2), synaptophysin (Cell Signaling Technology, #36406; 1:25; Milk-free diluent), vGLUT1 (Synaptic Systems, SYSY13503; 1:2000; Diluent 2); Homer1 (GeneTex,

GTX103278; 1:10; Diluent 2); anti-APP C-terminal fragment (BioLegend, #802801; 1: 25; Diluent 2) and β-actin (Santa Cruz Biotechnology, sc-47778; 1:100; Milk-free/diluent 2). Proteins were visualized using fluorescence and chemiluminescence.

#### Plasma testosterone and estradiol ELISAs

At euthanasia, whole blood was collected into an EDTA-coated syringe, spun down and plasma collected. Plasma analysis ELISAs were performed using either testosterone (R&D #KGE010) or estradiol (R&D Systems #KGE014) parameter assay kits following the manufacturer's instructions. Data are displayed in either pg or ng hormone per ml plasma.

#### Statistical analysis

Unless otherwise stated, two-way ANOVAs were performed. Three-way ANOVAs were also performed when the transgene (5xFAD) in addition to gonads and chromosomes were present as variables. For the main figures, interaction (or transgene), gonads and sex chromosomes as variables for two or three-way ANOVA are indicated in boxes beneath the data (interaction = I; gonads = G; and chromosome = C). A supplementary table contains exact P values for the main figures. Results of Tukey post-hoc test for multiple corrections on either two-or three-way ANOVAs are indicated in the Figures. P-value significance levels were determined as follows: $^{*}p < 0.05$, $^{**}p < 0.01$, $^{***}p < 0.001$ and $^{****}p < 0.0001$. Outliers were excluded based on the Grubbs outlier test. Each data point represents an individual mouse. All statistical tests used Graphpad Prism. All data were assumed to be normally distributed, but we did not formally test this. The experimental design in Fig. 1A was created using *BioRender*.

## Results

To distinguish the contributions of gonadal hormones and sex chromosomes to sex differences in AD pathology, we used the Four Core Genotypes (FCG) mouse model. This strain contains both a naturally occurring deletion of the testes-determining *Sry* gene from the Y chromosome ($Y^{-Sry}$), and a transgene containing the *Sry* gene ($Sry^{+}$) integrated on chromosome 3 [2]. Effects mediated by sex chromosomes and gonads are separated by the four resulting genotypes: ovary-bearing XX mice (XXO), ovary-bearing $XY^{-Sry}$ mice ($XY^{-}O$), testes-bearing $XXSry^{+}$ mice (XXT) or testes-bearing $XY^{-Sry}Sry^{+}$ mice ($XY^{-}T$).

$XY^{-}T$ mice were bred to transgene-positive 5xFAD females to produce 5xFAD; FCG offspring (Fig. 1A). Mice were left gonadally intact to circumvent potential modulation of AD pathology associated with gonadectomy and to assess the contribution of circulating sex hormones [45]. Plaque burden, neuroinflammation and neuronal survival were assessed at 4 and 8 months of age. FCG genotype did not alter plasma estradiol or testosterone levels at either age (Supplemental Figs. 1A, 1B and Supplemental Fig. 2A, 2B, respectively).

#### Sex chromosomes and gonads influence cortical plaque burden, gliosis and neuroinflammation in 4-month-old 5xFAD; FCG mice

Like human patients, the 5xFAD model exhibits sex differences in amyloid plaque burden [8, 18, 32]. We first determined the contribution of sex chromosomes and gonads on amyloid pathology in 4-month-old (4 m) 5xFAD,FCG mice via immunohistochemistry (IHC)—with red and blue bars representing this timepoint in 5xFAD; FCG groups. The cortex and subiculum were selected as they exhibit the most plaque deposition and related pathology in this model [31]. Using 6E10 to detect intraneuronal and dense-core Aβ, we observed XXO cortex showed significantly greater 6E10 immunoreactive area (IRA,depicted in graphs as percent coverage) and plaque number than $XY^{-}T$ cortex (Fig. 1B, Ci and ii), consistent with prior reports [18, 32]. Both gonads and chromosomes affected 6E10 IRA. Relative to XXO, $XY^{-}O$ and XXT mice had significantly less cortical 6E10 IRA and plaques (Fig. 1C). Aβ protein measured by capillary-assisted immunoblot electrophoresis confirmed the immunohistochemical findings (Fig. 1Di). Interestingly, C-terminal fragment (CTF) APP expression also showed similar trends as Aβ (Fig. 1Dii). No differences were observed in the subiculum across genotypes (Supplemental Fig. 1C).

The 5xFAD model displays robust gliosis with some sex differences [18]. We used GFAP and IBA1 IHC to assess astrogliosis and microgliosis, respectively. Cortical IRAs for GFAP and IBA1 were significantly higher in XXO versus $XY^{-}T$ mice (Fig. 1E, F respectively). Significant effects of both chromosomes and gonads were observed for cortical GFAP, but there was no interaction between them (Fig. 1E). Only sex chromosomes impacted cortical IBA1 IRA (Fig. 1F). However, both gonads and chromosomes affected the number of cortical IBA1 + cells (Fig. 1G), with significantly fewer IBA1 + cells in $XY^{-}O$ relative to XXO mice and in $XY^{-}T$ relative to their XXT counterparts (Fig. 1G). No significant chromosomal or gonadal effects were observed in the subiculum for GFAP or IBA1 IRA (Supplementary Fig. 1D, E), but chromosomes attenuated the number of IBA1 + cells, especially in $XY^{-}O$ and $XY^{-}T$ relative to XX mice (Supplementary Fig. 1F).

To exclude confounding results associated with the detection of full-length amyloid precursor protein (fl-APP) by 6E10, we used MOAB-2 to detect the

monomeric, oligomeric and fibrillar N-terminal residues in Aβ40 and Aβ42 [46]. MOAB-2 IHC (Fig. 1Hi, ii) produced comparable results in plaque number and overall burden. XXO mice had the greatest plaque number and burden, and both chromosomes and gonads significantly affected plaque number and burden. Interestingly, XXT mice had significantly fewer plaques and reduced plaque burden relative to XXO mice, trends shared by XY⁻O and XY⁻T animals. In the subiculum, both gonads and chromosomes influenced MOAB-2 coverage. Furthermore, MOAB-2 coverage was significantly decreased in XY⁻T relative to XXO mice (Supplementary Fig. 1G). We additionally measured the microglial lysosomal marker CD68 (Fig. 1I). CD68 upregulation signifies phagocytic microglia, and its expression is associated with Aβ internalization, degradation and subsequent clearance [22, 30]. We did not observe significant changes in CD68 expression (Fig. 1J), percent overlap of CD68 and 6E10 (Fig. 1K) or the number of microglia per plaque across genotypes (Fig. 1L). Similarly, no changes in these metrics were observed in the subiculum (Supplementary Fig. 1 V).

We further interrogated the neuroinflammatory milieu by performing quantitative PCR (qPCR) on cortical homogenates. There were no significant differences in gene expression between wildtype FCG mice (Supplemental Fig. 1H–M), but induced gene expression in 5xFAD mice depended on the interaction between chromosomes and gonads. 5xFAD; XY⁻T mice showed a significantly greater increase in *Iba1* than their XXT and XY⁻O counterparts (Fig. 1M). Increases in *Trem2*, *Gfap* and *Il-1b* were comparable in XXO, XY⁻O, and XY⁻T 5xFAD mice, but 5xFAD; XXT mice failed to increase *Trem2* (Fig. 1N), *Gfap* (Fig. 1O) or *Il-1b* (Fig. 1P) to the same extent as their XXO counterparts. *Tnfa* and *apolipoprotein E* (*Apoe*) were unaffected by FCG genotype (Fig. 1Q, R).

#### Sex chromosomes and gonads impact plaque remodeling and neuritic dystrophy in 4-month-old 5xFAD; FCG mice

Microglia provide a protective barrier around plaques, modifying the perimeter to prevent plaque-associated neurotoxicity and neuritic dystrophy [10]. Given the differences in cortical microglia, we wondered whether plaque remodeling was similarly affected by sex chromosomes and circulating hormones. To test this, we classified plaques based on morphology and compaction [28, 42, 47].

In the cortex, both sex chromosomes and gonads significantly affected the proportion of plaques that were filamentous or compact, whereas only gonads affected the proportion of inert plaques. XXO mice had a significantly higher proportion of compact plaques versus XY⁻T mice (Fig. 2A and Bii; full images shown in Supplementary Fig. 1 T), while the proportion of filamentous plaques was significantly higher in XY⁻T compared to XXO mice (Fig. 2Bii). Inert plaques comprised the smallest percentage of total plaque burden, with testes-bearing mice showing significantly fewer plaques of this type than XXO mice (Fig. 2Bi). The distribution of plaque morphology was unaffected in the subiculum (Supplementary Fig. 1U).

The effect of FCG genotype on X34 + plaques was consistent with 6E10 + and MOAB2 + plaques. There were fewer X34 + plaques and reduced size in XY⁻T compared to XXO mice (Fig. 2C, D). Relative to their XX counterparts, XY⁻ mice had fewer and smaller plaques, exhibiting a significant sex chromosome effect. In the subiculum, gonads and sex-chromosomes did not impact X34 plaque number (Supplementary Fig. 1N). Cortical X34 + plaque compaction was relatively unaffected by FCG genotype, but there was a trend towards increased compact X34 plaques in XY⁻T mice (Fig. 2E). In the subiculum, plaque compaction was similar across FCG genotypes (Supplementary Fig. 1O).

The 5xFAD model exhibits plaque-associated neuritic dystrophy [18] by 4 months of age. To test the impact of FCG genotype on neuritic dystrophy, we performed IHC for the neuron-associated dystrophic markers Lamp1, Ubiquitin and N-terminal APP (Nt-APP). The number of Lamp1 +, Ubiquitin + and Nt-APP + neurites were all lower in XY⁻T compared to XXO mice (Fig. 2F–H). Relative to XY⁻T mice, XXT mice had more dystrophic neurites of all types. This was not observed in ovary-bearing mice except for more Nt-APP + neurites in XXO compared to XY⁻O mice (Fig. 2H). Neuritic dystrophy markers were unaffected in the subiculum (Supplementary Fig. 1P-R). Additionally, FCG genotype did not affect neuronal survival in the subiculum of 5xFAD mice (Supplementary Fig. 1S).

Given the observed effects on plaques, microgliosis and neuritic dystrophy, we assessed the levels of cortical synaptic proteins (Fig. 2I–L). PSD95 and synaptophysin expression was significantly modulated by sex chromosomes in 5xFAD mice (Fig. 2I, J). Additionally, there was significantly more synaptophysin loss in 5xFAD; XY⁻T relative to 5xFAD; XXO mice (Fig. 2J). VGLUT2 in 5xFAD; XY⁻O mice was significantly lower than 5xFAD; XXO and 5xFAD; XXT mice (Fig. 2K) but no changes were observed in synaptic marker HOMER1 (Fig. 2L).

#### Cortical microgliosis, plaque burden and neuroinflammation in 8-month-old 5xFAD; FCG mice is largely affected by sex chromosomes

As 5xFAD mice exhibit worsened amyloid pathology at later timepoints [18], we repeated our analysis at 8 months of age to evaluate the contributions of

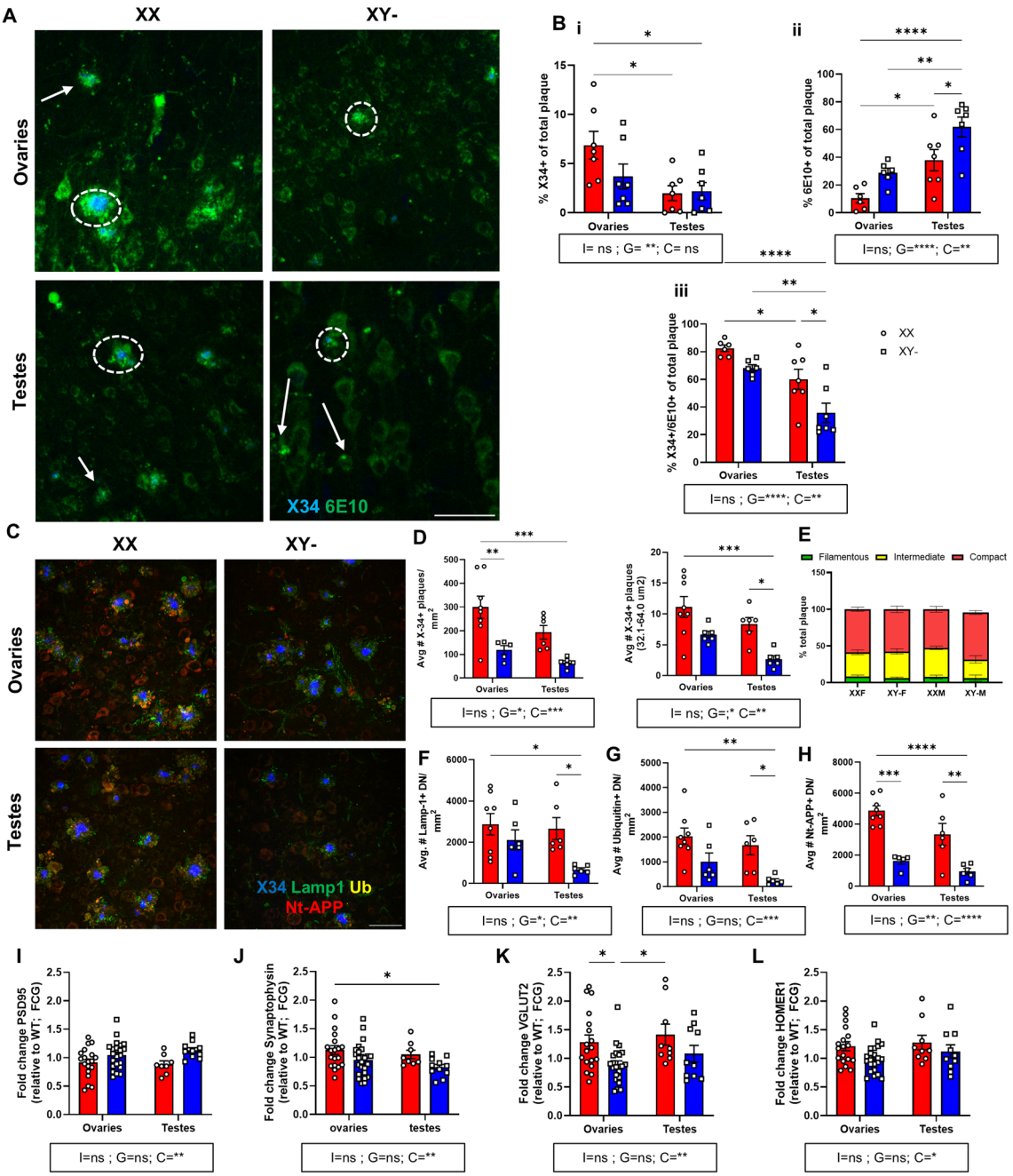


**Fig. 2** Testes reduce plaque burden and dystrophy and redistribute plaque morphologies in 4-month-old 5xFAD mice. **A** Representative images of 6E10 (green) and X34 (blue) in the cortex at 4-months of age. Arrow, 6E10 + plaques. White circles, X34/6E10 + plaques. Full images in Supplementary Fig. 1 T. **B** Percent X34 + (*i*), 6E10 + (*ii*) and X34 + /6E10 + plaques (*iii*) among total plaques. **C** Cortex stained for X34 (blue), Lamp1 (green), Ub (yellow) and Nt-APP (red). **D** *Left*, average number X34 positive plaques in the cortex. *Right*, average number cortical X34 plaques sized between 32.1 and 64 μm$^2$. **E** Cortical X34 plaque condensation among total X34 + plaques. Average number of cortical **F** Lamp1 + , **G** Ub + and **H** Nt-APP + dystrophic neurites (DN). **I** Fold changes for protein expression of PSD95, **J** synaptophysin, **K** VGLUT2 and **L** HOMER1 in the cortex for 5xFAD; FCG animals (normalized to respective WT FCG genotypes). Two-way ANOVA with Tukey post-hoc correction; ns = not significant. N ≥ 3 mice per group. Scale bars are 50 μm

sex chromosomes and gonads to disease progression (Fig. 3A)—with purple and green bars representing this time point in 5xFAD; FCG mice. Neither gonads nor sex chromosomes influenced cortical 6E10 IRA or plaque number based on IHC (Fig. 3B), but Aβ protein and CTF APP expression remained significantly elevated in

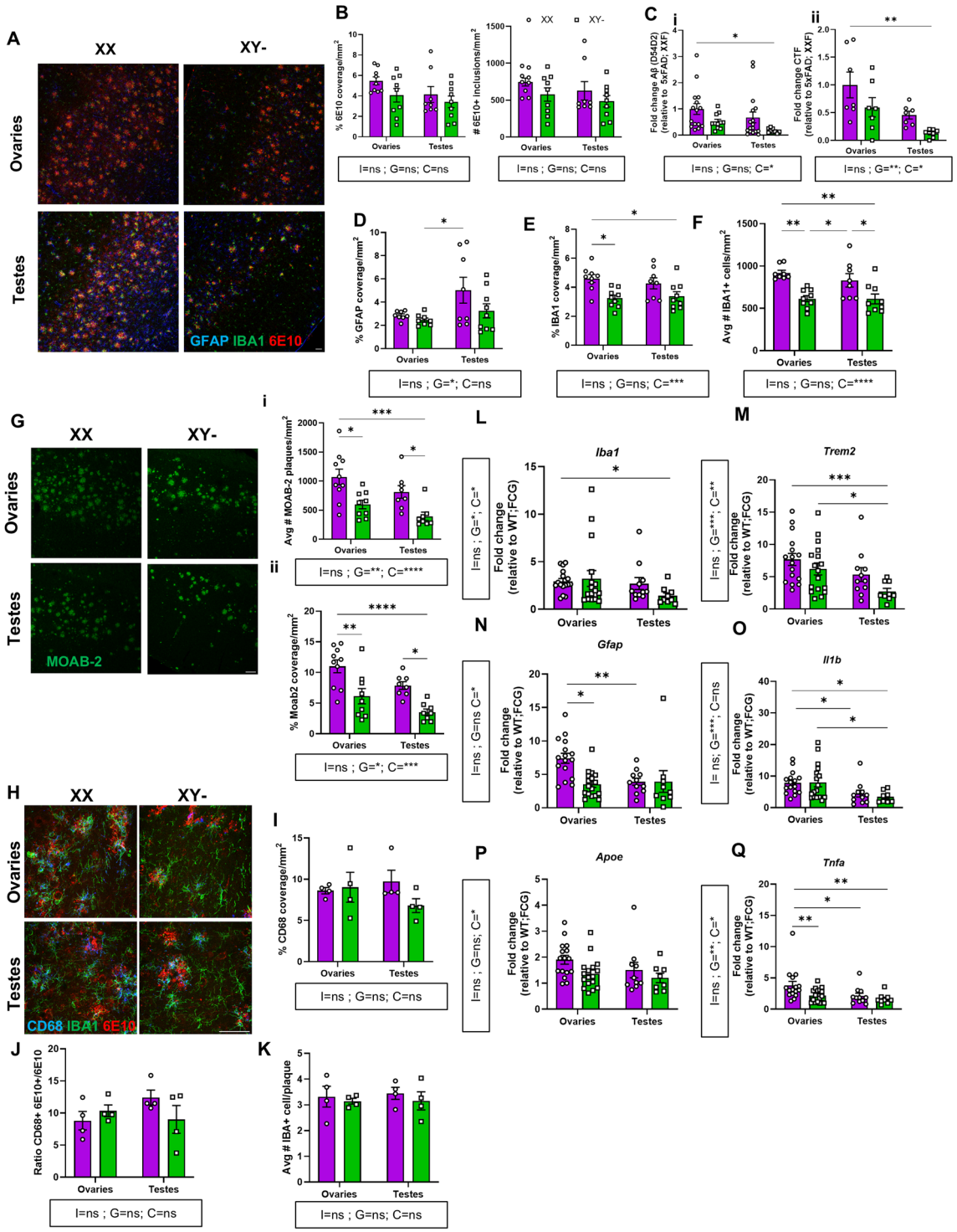


**Fig. 3** Distinct effects of chromosomes and gonads on plaque burden and microgliosis and neuroinflammation at 8-months. **A** Representative cortical images for GFAP (blue), IBA1 (green) and 6E10 (red). **B** Percent 6E10 + positive cortical plaque coverage and average number of plaques. **C** *i*, fold change cortical Aβ protein expression; *ii*, fold change cortical APP C-terminal fragment (CTF) protein expression. **D** Percent cortical GFAP coverage. **E** Percent cortical IBA1 coverage. **F** Average number cortical IBA1 + cells. **G** Representative cortical MOAB-2 images (green). *i*, average number cortical MOAB-2 + plaques. *ii*, percent cortical MOAB-2 coverage. **H** Images of cortical IBA1 (green), 6E10 (red) and CD68 (blue) with percent CD68 (I), percent double positive CD68/6E10 normalized to 6E10 area (**J**) and average #IBA1 + cell per plaque (**K**). **L**–**Q** Fold changes relative to wildtype FCG animals of indicated mRNA cortical genes in 5xFAD; FCG animals. **L** *Iba1*, **M** *Trem2*, **N** *Gfap*, **O** *Il1b*, **P** *Apoe* and **Q** *Tnfa*. Two-way ANOVA with Tukey post-hoc correction significance indicated by brackets; ns = not significant. N ≥ 3 mice per group. Scale bars for images are 50 µm

5xFAD; XXO relative to 5xFAD; XY⁻T mice (Fig. 3Ci, ii). However, the gonads influenced cortical GFAP IRA (Fig. 3D). IBA1 IRA was significantly lower in XY⁻O relative to XXO mice but was comparable in testes-bearing mice (Fig. 3D). Significantly more cortical IBA1 + cells were observed in XX versus XY⁻ mice irrespective of gonads (Fig. 3E). Plaque burden in the subiculum was largely unaffected, but XXT mice had enhanced astrogliosis over their XXO counterparts (Supplementary Fig. 2C-D). In the subiculum, IBA1 IRA was significantly higher in XXT over XY⁻O mice, but IBA1 + microglial numbers were unaffected by FCG genotype (Supplementary Fig. 2E-F).

In contrast to 6E10 + plaques, sex chromosomes and gonads significantly influenced MOAB-2 + IRA and plaque number. There was greater MOAB-2 + plaque burden and number in XX relative to XY⁻ mice with either ovaries or testes (Fig. 3G). MOAB-2 + IRA was unaffected in the subiculum (Supplementary Fig. 2G). CD68 expression, overlap between CD68 and 6E10 or microglial plaque counts were unchanged in both the cortex (Fig. 3H–K) and subiculum at 8 months of age (Supplementary Fig. 2U).

Wildtype FCG mice continued to show few differences in cortical gene expression at 8 months of age (Supplemental Fig. 2H–M). Unlike 4-month-old 5xFAD, the induction of gene expression in 8-month-old 5xFAD mice depended on both sex chromosomes and gonads. There was a significant sex chromosomes effect on *Iba1*, with a larger increase in XXO than XY⁻T 5xFAD mice (Fig. 3L). Sex chromosomes and gonads impacted the induction of *Trem2*, with ovary-bearing mice showing greater increases than testes-bearing mice, particularly in 5xFAD; XY⁻T (Fig. 3M). Similar effects were observed in *Gfap*, with XY⁻O, XXM, and XY⁻M mice showing comparable increases, but significantly less than in XXO mice (Fig. 3N). Regardless of sex chromosome complement, testes-bearing mice upregulated *Il1b* and *Tnfa* to a significantly lower degree, relative to ovary-bearing animals of either sex chromosome complement, whereas *Apoe* was unaffected by FCG genotype (Fig. 3O–Q).

### Plaque remodeling, neuritic dystrophy and neuron loss are influenced by sex chromosomes and gonads in 8-month-old 5xFAD; FCG mice

X34 + plaque number and size showed a sex-chromosome effect in the cortex, namely between XXO and XY⁻T mice (Fig. 4A–C). XXO and XY⁻O mice exhibited differences in X34 + plaque size (Fig. 4C). Distribution of cortical plaque compaction was unchanged across 5xFAD; FCG genotypes (Fig. 4D). There were no significant differences in dense-core plaque number, size or plaque compaction in the subiculum (Supplementary Fig. 2N-O). Plaque morphology in the cortex and subiculum were unaffected (Supplementary Fig. 2S-T).

Cortical dystrophy at 8 months of age resembled that at 4 months, with all markers significantly elevated in XXO compared to XY⁻T 5xFAD mice (Fig. 4E–G). In testes-bearing mice, the Y chromosome reduced dystrophy, with a trend in Lamp-1 + neurites (Fig. 4E), and significant decreases in Ubiquitin + and NtAPP + neurites (Fig. 4F, G). In the subiculum, FCG genotype did not affect dystrophic neurites (Supplementary Fig. 2P-R).

5xFAD mice exhibit neuronal loss in cortical Layer V at 8 months [31]. Given the effects on dystrophy, we investigated whether FCG genotype affected neuron survival. Wildtype FCG had comparable numbers of NeuN + cells in Layer V, and 5xFAD mice showed significantly reduced Layer V NeuN + numbers across FCG genotypes. 5xFAD,XY⁻T animals retained more NeuN + cells than both testes-bearing and ovary-bearing 5xFAD; XX animals (Fig. 4H). Changes in cortical synaptic protein levels were unaffected by FCG genotype (Fig. 4I–L).

Phagocytosis of amyloid alters microglial gene signatures, downregulating core genes and upregulating the expression of neurodegenerative markers such as CD11c [19, 26]. Since the microglial neurodegenerative phenotype has been observed in both male and female AD mouse models [19], and we noted microglia-specific alterations in 5xFAD,FCG animals, we tested whether sex chromosomes or circulating hormones regulated CD11c expression via IHC. CD11c was undetectable in 4-month-old 5xFAD; FCG mice (data not shown, but there was robust CD11c expression in cortical microglia associated with X34 + plaques at 8 months (Fig. 5A). The Y chromosome diminished CD11c + IRA and number in ovary-bearing, but not testes-bearing, 5xFAD; FCG mice (Fig. 5B, C). We also measured homeostatic and disease-associated microglia and neurodegenerative microglial genes [13, 26, 27] via qPCR in the cortex. While we observed few changes in homeostatic markers (Fig. 5D), significant overexpression of *cd11c* and *cst7* in 5xFAD; XXT versus 5xFAD; XY⁻T mice was observed along with overexpression of all these markers in 5xFAD; XY⁻O versus 5xFAD; XY⁻T mice (Fig. 5E). Wildtype FCG animals showed no differences in any of these markers (Supplementary Fig. 2 V).

## Discussion

We show both sex chromosomes and hormones from intact gonads modulate disease pathology in 5xFAD animals. In general, two X chromosomes increased microgliosis, plaque burden, and neuritic dystrophy, while testes blunted pathology. However, the magnitude of these effects varied across disease stages and brain regions. Our findings in cortical microglia and

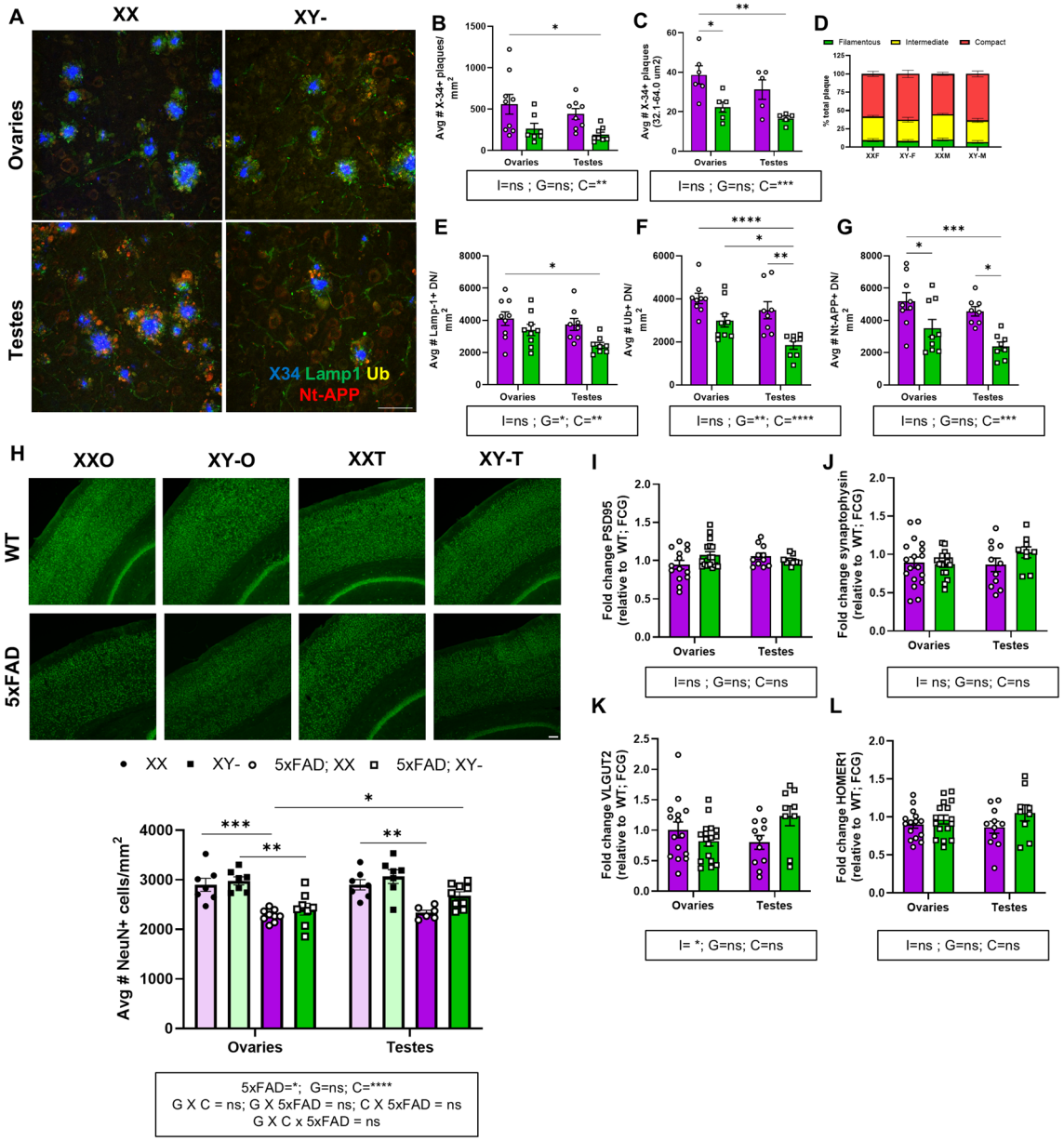


**Fig. 4** Testes abrogate cortical neuritic dystrophy and promote cortical neuron retention at 8-months of age. **A** Representative cortical images of X34 (blue), Lamp1 (green), Ub (yellow) and Nt-APP (red). **B** Average number of X34 cortical plaques. **C** Average number of cortical X34 plaques sized between 32.1 and 64 $\mu m^2$. **D** Cortical X34 plaque condensation among total X34 + plaques. **E** Lamp1 +, **F** Ubiquitin + or **G** Nt-APP + average dystrophic neurites (DN). **H** Images and average number of NeuN + (green) cells per unit area of Layer V. Three-way ANOVA with Tukey post-hoc correction for multiple comparisons. **I** Fold changes of PSD95, **J** synaptophysin, **K** VGLUT2 and **L** HOMER1 protein expression in 5xFAD; FCG animals relative to respective FCG genotypes. Two-way ANOVA with Tukey post-hoc correction significance indicated by brackets; ns = not significant. N ≥ 3 mice per group. Scale bars for images are 50 µm

gene expression suggest an amyloid-driven regulation of microglial phenotype, which is further defined by both sex chromosomes and gonads. Microglial phenotypes exist on a continuum in both male and female AD mouse models as well as in humans [19, 35]. Neuritic dystrophy triggered by amyloid plaques induces microglial neurodegenerative phenotypes characterized by upregulation of CD11c expression [26, 27]. CD11c has been shown to be upregulated at the protein level in microglia of 5xFAD animals [16, 41]. The functional impacts of CD11c upregulation on plaque-proximal microglia are unclear, but neonatal murine microglia express

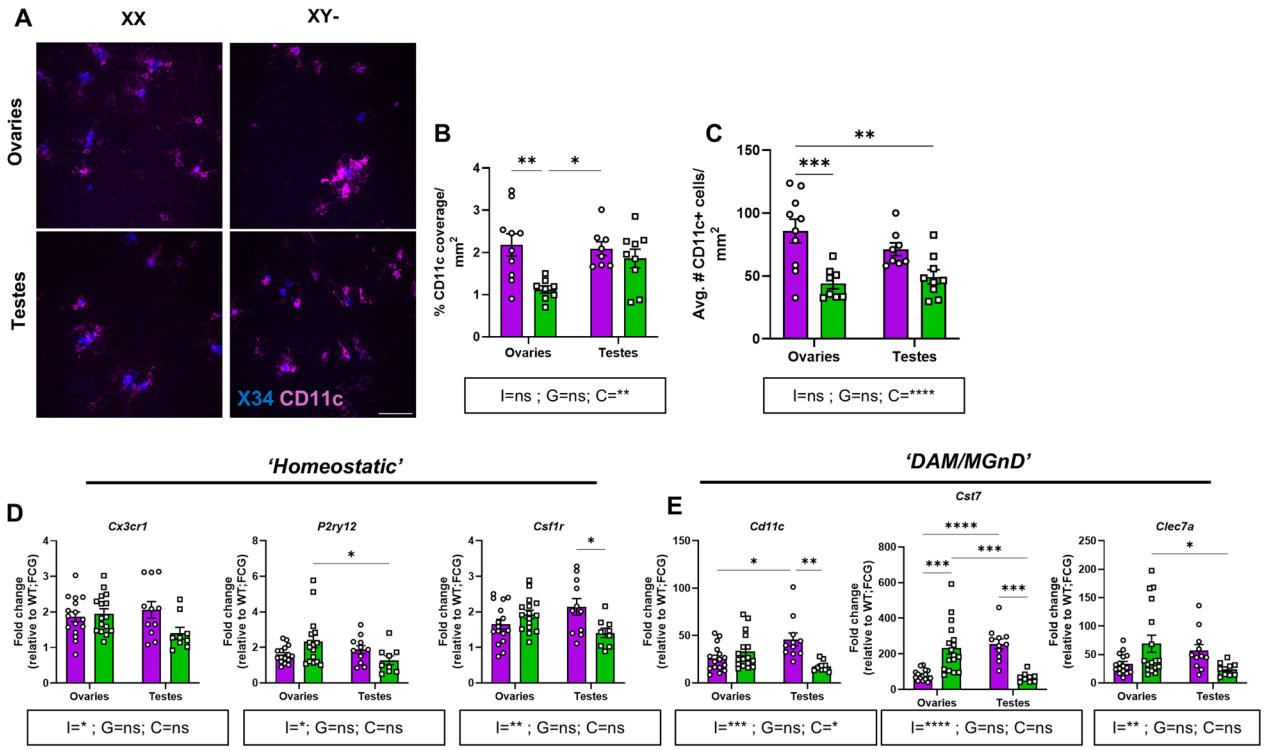


**Fig. 5** The Y chromosome limits cortical CD11c + microgliosis but its presence upregulates disease-associated microglial markers in ovary-bearing 5xFAD; XY- animals. **A** Representative cortical CD11c (magenta) and X34 + (blue) images. **B** Percent cortical CD11c + coverage. **C** Average number of cortical CD11c + microglia. **D** Cortical expression of homeostatic genes *cx3cr1*, *p2ry12* and *csf1r* and **E** DAM/MGnD genes *cd11c*, *cst7* and *clec7a* relative to WT; FCG genotypes. Two-way ANOVA with Tukey post-hoc correction significance indicated by brackets; ns = not significant. N ≥ 3 mice per group. Scale bar 50 µm

CD11c associated with the regulation of myelinogenesis and neurogenesis [43]. Additionally, CD11c + microglia regulate white matter repair in a mouse model of ischemic stroke [24]. Our studies on CD11c imply that, through either chromosomes or circulating hormones, sex-specific developmental gene expression repertoires may reactivate in microglia during neurodegenerative diseases. Additionally, our data suggest that sex chromosomes and gonads more selectively impact microglia than astrocytes, and that these responses are shaped by disease course in 5xFAD animals.

Plaque compaction is correlated with degree of neuritic dystrophy and microglia density [9, 10, 47]. Diffuse 6E10 + plaques correlate with higher dystrophy, while compact 6E10 + X34 + plaques correlate with less dystrophy on a per plaque basis. Our findings imply that the enhanced microgliosis and microglial numbers observed in XXO mice may result in more efficient plaque remodeling even though neuritic dystrophy is elevated in these animals.

While CD68 activation and ratio of CD68/6E10 overlap were unchanged across animals, pointing to sufficient microglial phagocytosis of fibrillar amyloid across genotypes, sex chromosomes and gonads may alter microglial uptake of soluble amyloid species through differential expression of microglial lipoprotein expression and alteration of apolipoprotein dynamics. The latter may lend to possible nuanced mechanisms distinguishing male and female microglia in the 5xFAD; FCG model.

Another microglial neurodegenerative phenotypic marker is *Apoe* [13]. *APOE* has been associated with a sex bias in disease manifestations in women with AD, mostly due to sex-specific gene expression [14, 15]. Aside from ApoE's effects on clearance of soluble amyloid [25], microglia also seed ApoE into plaques to facilitate amyloid-plaque compaction [36, 39]. Our data suggest *Apoe* most likely serves to facilitate microglial plaque compaction early during disease in 5xFAD mice. It will be important for future experiments to address the protein localization of ApoE (e.g.: in dense-core plaques) in 5xFAD; FCG animals. We noticed in 8-month-old animals that the Y chromosome upregulated some genes associated with the microglial neurodegenerative phenotypes, such as *cst7* [13], but only when intact ovaries were present (Fig. 5). On the other hand, testes universally blunted neurodegenerative phenotype markers but only

in mice with one X chromosome whereas homeostatic markers were largely unaffected (Fig. 5).

Inactivation of the second X chromosome is a mammalian regulatory mechanism to normalize expression levels of X chromosome-related genes and microRNAs [23]. Epigenetic mechanisms also dictate X chromosome gene expression and stability [4]. Genes escaping X inactivation can promote greater gene dosage in females, and dysregulation of X-chromosome inactivation occurs in both aging and AD [17]. These mechanisms likely play roles in our study, and we show that the X chromosome actively shapes microglial responses to AD. Two X chromosomes promoted resilience to AD by regulating cognitive decline and mortality in humans and AD mouse models through sex-specific expression of histone demethylase *KDM6A* [11]. *KDM6A* likely regulates AD resilience in female neurons by modulating Aβ-induced neurotoxicity where it is overexpressed due to escape from X inactivation [11]. We did not see similar effects in neuron retention, which may be explained by experimental design. First, we left gonads intact to provide a source of circulating hormones to assess their impact on AD. Second, we used a mouse model that differed in its plaque deposition and neuronal loss time courses. Where the 5xFAD mouse model shows neuronal loss in several brain regions, the *hAPP* model in their study only exhibits neuron loss in the CA1 of the hippocampus [31, 44]. Furthermore, we utilized the pan-neuronal marker NeuN to analyze cortical neuronal density, whereas Wright and colleagues analyzed hippocampal density with the neuronal marker calbindin [44]. While others have demonstrated that sex chromosomes and hormones regulate pathology using the FCG in other mouse models of AD, our findings specifically implicate microglia and how sex chromosomes and gonads can produce divergent impacts on microglia, and thus amyloid-driven pathology [3, 11, 12, 29, 40].

We also observed brain-region specific effects. Depending on sex, rodent brain regions show different microglial densities and phenotypes that respond differentially to certain contexts, such as disease (reviewed in [37]). Microglia in the cortex and subiculum may possess different morphologies and transcriptomes in 5xFAD,FCG animals that are influenced by both sex chromosomes and sex hormones, but our study did not address microglial morphologies and transcriptomics. The lack of FCG effects in the subiculum may be largely due to higher plaque burden in that region versus the cortex [31]. Although human microglial AD studies are limited, brains from female AD patients showed greater plaque burden in certain regions, and female microglia were more complex than male microglia [20, 29]. In addition to a more thorough investigation of amyloid-induced pathology on brain regions other than the cortex and subiculum, further analysis of other cell types, such as astrocytes, and pathology in other brain regions will be critical in discerning potential sex-chromosome and gonad-driven effects on amyloid pathology. Nonetheless, the data we report here is consistent with other mouse models showing sexual dimorphism in pathology and human AD studies.

We show that possession of two X chromosomes enhances microgliosis, with ovaries exerting a greater effect than testes. Conversely, one X chromosome can abrogate amyloid-related pathology in either ovary-or testes-bearing animals. Microgliosis and microglial phenotypes were correlated with enhanced amyloid-related pathology, suggestive of microglia-mediated modification of AD that is dependent on both sex chromosomes and sex hormones. Our findings highlight the nuanced interplay between sex chromosomes and circulating sex hormones from the gonads in modulating AD pathology.

**Abbreviations**

| | |
|---|---|
| FCG | Four-core genotype |
| XXO | Ovary-bearing XX |
| XY-O | Ovary-bearing $XY^{-Sry}$ |
| XXT | Testes-bearing $XXSry^{+}$ |
| XY-T | Testes-bearing $XY^{-Sry}Sry^{+}$ |
| Aβ | β-Amyloid |
| IHC | Immunohistochemistry |
| IRA | Immunoreactive area |
| fl-APP | Full-length amyloid precursor protein |
| IBA1 | Ionized calcium-binding adaptor molecule-1 |
| GFAP | Glial fibrillary acidic protein |
| Ub | Ubiquitin |
| Nt-APP | N-terminal amyloid precursor protein |
| DN | Dystrophic neurites |
| PSD95 | Postsynaptic density protein 95 |

## Supplementary Information

The online version contains supplementary material available at https://doi.org/10.1186/s12974-025-03404-8.

Supplementary material 1: Figure 1: FCG and 5xFAD; FCG plasma hormone concentrations and subicular plaque burden, gliosis, neuroinflammation, neuritic dystrophy, neuronal retention and plaque compaction in FCG and 5xFAD; FCG animals at 4-months old. (A) Plasma ELISA estradiol concentration levels (pg/mL) in ovary-bearing FCG and 5xFAD: FCG animals (interaction P = 0.4711, ns; transgene P = 0.6148, ns; chromosome P = 0.7326, ns). (B) Plasma ELISA testosterone concentration (ng/mL) in testes-bearing FCG and 5xFAD; FCG animals (interaction P = 0.3681, ns; transgene P = 0.9516, ns; chromosome P = 0.0379, *). (C) Percent 6E10+ coverage (interaction P = 0.2290, ns; gonads P = 0.6118, ns; chromosome P = 0.8481, ns). (D) Percent GFAP coverage (interaction P = 0.7851, ns; gonads P = 0.0053, **; chromosome P = 0.5869, ns). (E) Percent IBA1 coverage (interaction P = 0.4301, ns; gonads P = 0.9393, ns; chromosome P = 0.0092, **) per unit area. (F) Average number of IBA1+ cells (interaction P = 0.4573, ns; gonads P = 0.3324, ns; chromosome P = 0.0042, **) per unit area in the subiculum. (G) Percent subicular MOAB-2 coverage (interaction P = 0.8201, ns; gonads P = 0.0412, *; chromosome P = 0.0379, *). (H-M) Fold changes of indicated mRNA cortical gene expression in FCG animals. (H) *Iba1* (interaction P =0.4446, ns; gonads P = 0.0336, *; chromosome P = 0.6935, ns). (I) *Trem2* (interaction P = 0.7918, ns; gonads P = 0.0953, ns; chromosome P = 0.9194, ns). (J) *Gfap* (interaction P = 0.2089, ns; gonads P = 0.3516, ns; chromosome P = 0.3859, ns). (K) *Apoe* (interaction P =

0.5097, ns; gonads P = 0.2193, ns; chromosome P = 0.8214, ns). (L) *Il1b* (interaction P = 0.6686, ns; gonads P = 0.2593, ns; chromosome P = 0.4673, ns). (M) *Tnfa* (interaction P = 0.9934, ns; gonads P = 0.0676, ns; chromosome P = 0.3698, ns). (N) *Left*. Average number of X34+ plaques in the subiculum (interaction P = 0.3469, ns; gonads P = 0.1352, ns; chromosome P = 0.1140, ns). *Right*. Average number of X34+ plaques sized between 32.1 and 64 μm$^2$ (interaction P = 0.8679, ns; gonads P = 0.8881, ns; chromosome P = 0.1508, ns). (O) Relative distribution of filamentous, intermediate and compact X34 plaques among total plaques in the subiculum. No significant differences were observed between X34 plaque distributions. Average number of (P) Lamp1+ (interaction P = 0.8324, ns; gonads P = 0.4566, ns; chromosome P = 0.3905, ns), (Q) ubiquitin+ (interaction P = 0.1312, ns; gonads P = 0.7375, ns; chromosome P = 0.0060, **) and (R) Nt-APP+ (interaction P = 0.4425, ns; gonads P = 0.0377, *; chromosome P = 0.0933, ns) dystrophic neurites (DN). (S) Average # NeuN+ cells in the subiculum; three-way ANOVA with Tukey post-hoc correction for multiple comparisons. The following was a significant source of variation: chromosome, P < 0.0303, *. The other sources of variation were not significant. (T) Full images with white box indicates enlarged image shown in Figure 2A. Scale bar 50 μm. (U) Quantification of subicular plaque species represented as percent total plaque. *Left*: X34+ plaques (interaction P = 0.1796, ns; gonads P = 0.0838, ns; chromosome P = 0.0534, ns); *middle*: 6E10+ plaques (interaction P = 0.4093, ns; gonads P = 0.2957, ns; chromosome P = 0.6931, ns); and *right*: X34+/6E10+ plaques (interaction P = 0.6780, ns; gonads P = 0.7735, ns; chromosome P = 0.6761, ns). (V) Subicular coverage of CD68 (interaction P = 0.6048, ns; gonads P = 0.4247, ns; chromosome P = 0.1653, ns), double-positive CD68/6E10 (interaction P =0.3123, ns; gonads P = 0.6569, ns; chromosome P = 0.8803, ns) and average number of IBA1+ cells per plaque (interaction P = 0.4818, ns; gonads P = 0.0193, *; chromosome P = 0.7938, ns). Each data point represents an individual mouse. Two-way ANOVA with Tukey post-hoc correction significance indicated by brackets; ns = not significant. N≥3 mice per group.

Supplementary material 2: Figure 2: FCG and 5xFAD; FCG plasma hormone concentrations and subicular plaque burden, gliosis, neuroinflammation, neuritic dystrophy and plaque compaction in FCG and 5xFAD; FCG animals at 8-months old. (A) Plasma ELISA estradiol concentration levels (pg/mL) in ovary-bearing FCG and 5xFAD: FCG animals (interaction P = 0.9094, ns; transgene P = 0.0454, *; chromosome P = 0.7217, ns). (B) Plasma ELISA testosterone concentration (ng/mL) in testes-bearing FCG and 5xFAD; FCG animals (interaction P = 0.6450, ns; transgene P = 0.1176, ns; chromosome P = 0.6281, ns). (C-F) Subicular quantifications of immunohistochemistry stains. (C) Percent 6E10+ coverage (interaction P = 0.6760, ns; gonads P = 0.3966, ns; chromosome P = 0.8255, ns), (D) percent GFAP coverage (interaction P = 0.4522, ns; gonads P = 0.0036, **; chromosome P = 0.5892, ns), (E) percent IBA1 coverage (interaction P = 0.4477, ns; gonads P = 0.1102, ns; chromosome P = 0.0073, **), (F) Average number of IBA1+ cells (interaction P = 0.6408, ns; gonads P = 0.2716, ns; chromosome P = 0.0210, *) and (G) Percent MOAB-2 coverage in the subiculum (interaction P = 0.5481, ns; gonads P = 0.1276, ns; chromosome P = 0.0996, ns) per unit area. (I-M) Fold changes of indicated mRNA cortical gene expression in FCG animals. (I) *Iba1* (interaction P = 0.4446, ns; gonads P = 0.0336, *; chromosome P = 0.6935, ns). (J) *Trem2* (interaction P = 0.7918, ns; gonads P = 0.0953, ns; chromosome P = 0.9194, ns). (K) *Gfap* (interaction P = 0.2089, ns; gonads P = 0.3516, ns; chromosome P = 0.3859, ns). (L) *Apoe* (interaction P = 0.5097, ns; gonads P = 0.2193, ns; chromosome P = 0.8214, ns). (M) *Il1b* (interaction P = 0.6686, ns; gonads P = 0.2596, ns; chromosome P = 0.4673, ns). (N) *Tnfa* (interaction P = 0.9934, ns; gonads P = 0.0676, ns; chromosome P = 0.3698, ns). (N) *Left*. Average number of subicular X34+ plaques (interaction P = 0.3530, ns; gonads P = 0.3018, ns; chromosome P = 0.4042, ns). *Right*. Number of X34+ plaques sized between 32.1 and 64 μm$^2$ (interaction P = 0.0370, *; gonads P = 0.9891, ns; chromosome P = 0.4784, ns). (O) Relative distribution of X34+ filamentous, intermediate and compact-like plaques among total plaques in the subiculum. No significant differences were observed among X34+ plaque condensation types. Average number of (P) Lamp1+ (interaction P = 0.4299, ns; gonads P = 0.1462, ns; chromosome P = 0.6032, ns), (Q) ubiquitin+ (interaction P = 0.3012, ns; gonads P = 0.1031, ns; chromosome P = 0.6582, ns) and (R) Nt-APP+ (interaction P = 0.8642, ns; gonads P = 0.7363, ns; chromosome P = 0.6728, ns) dystrophic neurites in the subiculum. (S) Quantification of cortical plaque species represented as percent total plaque at 8-months of age. *Left*: X34+ plaques (interaction P = 0.0798, ns; gonads P = 0.5694, ns; chromosome P = 0.6626, ns); *middle*: 6E10+ plaques (interaction P = 0.6343, ns; gonads P = 0.3364, ns; chromosome P = 0.6452, ns); and *right*: X34+/6E10+ plaques (interaction P = 0.0942, ns; gonads P = 0.6363, ns; chromosome P = 0.6911, ns). (T) Quantification of subicular plaque species represented as percent total plaque. *Left*: X34+ plaques (interaction P = 0.2334, ns; gonads P = 0.4118, ns; chromosome P = 0.1322, ns); *middle*: 6E10+ plaques (interaction P = 0.7902, ns; gonads P = 0.6869, ns; chromosome P = 0.1796, ns); and *right*: X34+/6E10+ plaques (interaction P = 0.2599, ns; gonads P = 0.4919, ns; chromosome P = 0.0938, ns). (U) Subicular coverage of CD68 (interaction P = 0.7731, ns; gonads P = 0.5125, ns; chromosome P = 0.9220, ns), double-positive CD68/6E10 (interaction P =0.4154, ns; gonads P = 0.1897, ns; chromosome P = 0.8719, ns) and average number of IBA1+ cells per plaque (interaction P = 0.7410, ns; gonads P = 0.9513, *; chromosome P = 0.9670, ns). (V) Wildtype expression of indicated cortical genes. Each data point represents an individual mouse. Two-way ANOVA with Tukey post-hoc correction significance indicated by brackets; ns= not significant. N≥3 mice per group.

Supplementary material 3: Table 1 Table containing exact P values for Two-Way ANOVA factors used in the main figures.

**Acknowledgements**
We thank P.R. Keller-Norrell for designing the 5xFAD; FCG diagram.

**Author contributions**
BTC, LL, OB, HZ, EM and EGR performed experiments. BTC, OB and EGR analyzed data. BC and EGR wrote the manuscript. All authors read and approved the final manuscript.

**Funding**
This work was supported by the National Institute on Aging of the National Institutes of Health (Award Number R01AG075897 to E.G. Reed), the donors of Alzheimer's Disease Research, a program of BrightFocus Foundation (A2021036S to E.G. Reed) and institutional funds (to E.G. Reed).

**Availability of data and materials**
The data contained and analyzed in this study are available upon reasonable request from the corresponding author.

## Declarations

**Ethics approval and consent to participate**
All animal procedures were approved by the Institutional Animal Care and Use Committee at NEOMED.

**Consent for publication**
Not applicable.

**Competing interests**
The authors declare no competing interests.

Received: 27 September 2024 Accepted: 3 March 2025
Published online: 13 March 2025

**References**

1. Alzheimer's Disease Facts and Figures, 2024. Alzheimer's disease and dementia.
2. Arnold AP. Mouse models for evaluating sex chromosome effects that cause sex differences in non-gonadal tissues. J Neuroendocrinol. 2009;21:377–86. https://doi.org/10.1111/j.1365-2826.2009.01831.x.

3. Arnold AP. Four Core Genotypes and XY* mouse models: update on impact on SABV research. Neurosci Biobehav Rev. 2020;119:1–8. https://doi.org/10.1016/j.neubiorev.2020.09.021.
4. Bajic VP, Essack M, Zivkovic L, Stewart A, Zafirovic S, Bajic VB, Gojobori T, Isenovic E, Spremo-Potparevic B. The X files: "the mystery of x chromosome instability in Alzheimer's disease." Front Genet. 2020. https://doi.org/10.3389/fgene.2019.01368.
5. Barnes LL, Wilson RS, Bienias JL, Schneider JA, Evans DA, Bennett DA. Sex differences in the clinical manifestations of Alzheimer disease pathology. Arch Gen Psychiatry. 2005;62:685–91. https://doi.org/10.1001/archpsyc.62.6.685.
6. Bianchi I, Lleo A, Gershwin ME, Invernizzi P. The X chromosome and immune associated genes. J Autoimmun. 2012;38:J187–92. https://doi.org/10.1016/j.jaut.2011.11.012.
7. Bordt EA, Ceasrine AM, Bilbo SD. Microglia and sexual differentiation of the developing brain: a focus on ontogeny and intrinsic factors. Glia. 2020;68:1085–99. https://doi.org/10.1002/glia.23753.
8. Buckley RF, Mormino EC, Rabin JS, Hohman TJ, Landau S, Hanseeuw BJ, Jacobs HIL, Papp KV, Amariglio RE, Properzi MJ, Schultz AP, Kirn D, Scott MR, Hedden T, Farrell M, Price J, Chhatwal J, Rentz DM, Villemagne VL, Johnson KA, Sperling RA. Sex differences in the association of global amyloid and regional tau deposition measured by positron emission tomography in clinically normal older adults. JAMA Neurol. 2019;76:542–51. https://doi.org/10.1001/jamaneurol.2018.4693.
9. Casali BT, MacPherson KP, Reed-Geaghan EG, Landreth GE. Microglia depletion rapidly and reversibly alters amyloid pathology by modification of plaque compaction and morphologies. Neurobiol Dis. 2020;142:104956. https://doi.org/10.1016/j.nbd.2020.104956.
10. Condello C, Yuan P, Schain A, Grutzendler J. Microglia constitute a barrier that prevents neurotoxic protofibrillar Aβ42 hotspots around plaques. Nat Commun. 2015;6:6176. https://doi.org/10.1038/ncomms7176.
11. Davis EJ, Broestl L, Abdulai-Saiku S, Worden K, Bonham LW, Miñones-Moyano E, Moreno AJ, Wang D, Chang K, Williams G, Garay BI, Lobach I, Devidze N, Kim D, Anderson-Bergman C, Yu G-Q, White CC, Harris JA, Miller BL, Bennett DA, Arnold AP, De Jager PL, Palop JJ, Panning B, Yokoyama JS, Mucke L, Dubal DB. A second X chromosome contributes to resilience in a mouse model of Alzheimer's disease. Sci Transl Med. 2020;12:eaaz5677. https://doi.org/10.1126/scitranslmed.aaz5677.
12. Davis EJ, Solsberg CW, White CC, Miñones-Moyano E, Sirota M, Chibnik L, Bennett DA, De Jager PL, Yokoyama JS, Dubal DB. Sex-specific association of the X chromosome with cognitive change and tau pathology in aging and alzheimer disease. JAMA Neurol. 2021;78:1249–54. https://doi.org/10.1001/jamaneurol.2021.2806.
13. Deczkowska A, Keren-Shaul H, Weiner A, Colonna M, Schwartz M, Amit I. Disease-associated microglia: a universal immune sensor of neurodegeneration. Cell. 2018;173:1073–81. https://doi.org/10.1016/j.cell.2018.05.003.
14. Dumitrescu L, Barnes LL, Thambisetty M, Beecham G, Kunkle B, Bush WS, Gifford KA, Chibnik LB, Mukherjee S, De Jager PL, Kukull W, Crane PK, Resnick SM, Keene CD, Montine TJ, Schellenberg GD, Deming Y, Chao MJ, Huentelman M, Martin ER, Hamilton-Nelson K, Shaw LM, Trojanowski JQ, Peskind ER, Cruchaga C, Pericak-Vance MA, Goate AM, Cox NJ, Haines JL, Zetterberg H, Blennow K, Larson EB, Johnson SC, Albert M, Bennett DA, Schneider JA, Jefferson AL, Hohman TJ. Sex differences in the genetic predictors of Alzheimer's pathology. Brain. 2019;142:2581–9. https://doi.org/10.1093/brain/awz206.
15. Dumitrescu L, Mayeda ER, Sharman K, Moore AM, Hohman TJ. Sex differences in the genetic architecture of Alzheimer's disease. Curr Genet Med Rep. 2019;7:13–21. https://doi.org/10.1007/s40142-019-0157-1.
16. Ennerfelt H, Frost EL, Shapiro DA, Holliday C, Zengeler KE, Voithofer G, Bolte AC, Lammert CR, Kulas JA, Ulland TK, Lukens JR. SYK coordinates neuroprotective microglial responses in neurodegenerative disease. Cell. 2022;185:4135-4152.e22. https://doi.org/10.1016/j.cell.2022.09.030.
17. Fang H, Deng X, Disteche CM. X-factors in human disease: impact of gene content and dosage regulation. Hum Mol Genet. 2021;30:R285–95. https://doi.org/10.1093/hmg/ddab221.
18. Forner S, Kawauchi S, Balderrama-Gutierrez G, Kramár EA, Matheos DP, Phan J, Javonillo DI, Tran KM, Hingco E, da Cunha C, Rezaie N, Alcantara JA, Baglietto-Vargas D, Jansen C, Neumann J, Wood MA, MacGregor GR, Mortazavi A, Tenner AJ, LaFerla FM, Green KN. Systematic phenotyping and characterization of the 5xFAD mouse model of Alzheimer's disease. Sci Data. 2021;8:270. https://doi.org/10.1038/s41597-021-01054-y.
19. Grubman A, Choo XY, Chew G, Ouyang JF, Sun G, Croft NP, Rossello FJ, Simmons R, Buckberry S, Landin DV, Pflueger J, Vandekolk TH, Abay Z, Zhou Y, Liu X, Chen J, Larcombe M, Haynes JM, McLean C, Williams S, Chai SY, Wilson T, Lister R, Pouton CW, Purcell AW, Rackham OJL, Petretto E, Polo JM. Transcriptional signature in microglia associated with Aβ plaque phagocytosis. Nat Commun. 2021;12:3015. https://doi.org/10.1038/s41467-021-23111-1.
20. Guillot-Sestier M-V, Araiz AR, Mela V, Gaban AS, O'Neill E, Joshi L, Chouchani ET, Mills EL, Lynch MA. Microglial metabolism is a pivotal factor in sexual dimorphism in Alzheimer's disease. Commun Biol. 2021;4:1–13. https://doi.org/10.1038/s42003-021-02259-y.
21. Guneykaya D, Ivanov A, Hernandez DP, Haage V, Wojtas B, Meyer N, Maricos M, Jordan P, Buonfiglioli A, Gielniewski B, Ochocka N, Cömert C, Friedrich C, Artiles LS, Kaminska B, Mertins P, Beule D, Kettenmann H, Wolf SA. Transcriptional and translational differences of microglia from male and female brains. Cell Rep. 2018;24:2773-2783.e6. https://doi.org/10.1016/j.celrep.2018.08.001.
22. Henjum K, Årskog V, Jendresen CB, Fladby T, Torp R, Nilsson LNG. Analyzing microglial-associated Aβ in Alzheimer's disease transgenic mice with a novel mid-domain Aβ-antibody. Sci Rep. 2020;10:10590. https://doi.org/10.1038/s41598-020-67419-2.
23. Jégu T, Aeby E, Lee JT. The X chromosome in space. Nat Rev Genet. 2017;18:377–89. https://doi.org/10.1038/nrg.2017.17.
24. Jia J, Zheng L, Ye L, Chen J, Shu S, Xu S, Bao X, Xia S, Liu R, Xu Y, Zhang M. CD11c+ microglia promote white matter repair after ischemic stroke. Cell Death Dis. 2023;14:1–13. https://doi.org/10.1038/s41419-023-05689-0.
25. Jiang Q, Lee CYD, Mandrekar S, Wilkinson B, Cramer P, Zelcer N, Mann K, Lamb B, Willson TM, Collins JL, Richardson JC, Smith JD, Comery TA, Riddell D, Holtzman DM, Tontonoz P, Landreth GE. ApoE promotes the proteolytic degradation of Abeta. Neuron. 2008;58:681–93. https://doi.org/10.1016/j.neuron.2008.04.010.
26. Keren-Shaul H, Spinrad A, Weiner A, Matcovitch-Natan O, Dvir-Szternfeld R, Ulland TK, David E, Baruch K, Lara-Astaiso D, Toth B, Itzkovitz S, Colonna M, Schwartz M, Amit I. A unique microglia type associated with restricting development of Alzheimer's disease. Cell. 2017;169:1276-1290.e17. https://doi.org/10.1016/j.cell.2017.05.018.
27. Krasemann S, Madore C, Cialic R, Baufeld C, Calcagno N, El Fatimy R, Beckers L, O'Loughlin E, Xu Y, Fanek Z, Greco DJ, Smith ST, Tweet G, Humulock Z, Zrzavy T, Conde-Sanroman P, Gacias M, Weng Z, Chen H, Tjon E, Mazaheri F, Hartmann K, Madi A, Ulrich J, Glatzel M, Worthmann A, Heeren J, Budnik B, Lemere C, Ikezu T, Heppner FL, Litvak V, Holtzman DM, Lassmann H, Weiner HL, Ochando J, Haass C, Butovsky O. The TREM2-APOE pathway drives the transcriptional phenotype of dysfunctional microglia in neurodegenerative diseases. Immunity. 2017;47:566-581.e9. https://doi.org/10.1016/j.immuni.2017.08.008.
28. Lee CYD, Daggett A, Gu X, Jiang L-L, Langfelder P, Li X, Wang N, Zhao Y, Park CS, Cooper Y, Ferando I, Mody I, Coppola G, Xu H, Yang XW. Elevated TREM2 gene dosage reprograms microglia responsivity and ameliorates pathological phenotypes in Alzheimer's disease models. Neuron. 2018;97:1032-1048.e5. https://doi.org/10.1016/j.neuron.2018.02.002.
29. Lopez-Lee C, Torres ERS, Carling G, Gan L. Mechanisms of sex differences in Alzheimer's disease. Neuron. 2024;112:1208–21. https://doi.org/10.1016/j.neuron.2024.01.024.
30. Matsumura A, Suzuki S, Iwahara N, Hisahara S, Kawamata J, Suzuki H, Yamauchi A, Takata K, Kitamura Y, Shimohama S. Temporal changes of CD68 and α7 nicotinic acetylcholine receptor expression in microglia in Alzheimer's disease-like mouse models. J Alzheimers Dis. 2015;44:409–23. https://doi.org/10.3233/JAD-141572.
31. Oakley H, Cole SL, Logan S, Maus E, Shao P, Craft J, Guillozet-Bongaarts A, Ohno M, Disterhoft J, Eldik LV, Berry R, Vassar R. Intraneuronal β-amyloid aggregates, neurodegeneration, and neuron loss in transgenic mice with five familial Alzheimer's disease mutations: potential factors in amyloid plaque formation. J Neurosci. 2006;26:10129–40. https://doi.org/10.1523/JNEUROSCI.1202-06.2006.
32. Oblak AL, Lin PB, Kotredes KP, Pandey RS, Garceau D, Williams HM, Uyar A, O'Rourke R, O'Rourke S, Ingraham C, Bednarczyk D, Belanger M, Cope ZA, Little GJ, Williams S-PG, Ash C, Bleckert A, Ragan T, Logsdon BA, Mangravite LM, Sukoff Rizzo SJ, Territo PR, Carter GW, Howell GR, Sasner M, Lamb BT. Comprehensive evaluation of the 5XFAD mouse model for preclinical testing applications: a MODEL-AD study. Front Aging Neurosci. 2021. https://doi.org/10.3389/fnagi.2021.713726.

33. Ocañas SR, Pham KD, Cox JEJ, Keck AW, Ko S, Ampadu FA, Porter HL, Ansere VA, Kulpa A, Kellogg CM, Machalinski AH, Thomas MA, Wright Z, Chucair-Elliott AJ, Freeman WM. Microglial senescence contributes to female-biased neuroinflammation in the aging mouse hippocampus: implications for Alzheimer's disease. J Neuroinflamm. 2023;20:188. https://doi.org/10.1186/s12974-023-02870-2.
34. Palaszynski KM, Smith DL, Kamrava S, Burgoyne PS, Arnold AP, Voskuhl RR. A yin-yang effect between sex chromosome complement and sex hormones on the immune response. Endocrinology. 2005;146:3280–5. https://doi.org/10.1210/en.2005-0284.
35. Paolicelli RC, Sierra A, Stevens B, Tremblay M-E, Aguzzi A, Ajami B, Amit I, Audinat E, Bechmann I, Bennett M, Bennett F, Bessis A, Biber K, Bilbo S, Blurton-Jones M, Boddeke E, Brites D, Brône B, Brown GC, Butovsky O, Carson MJ, Castellano B, Colonna M, Cowley SA, Cunningham C, Davalos D, De Jager PL, de Strooper B, Denes A, Eggen BJL, Eyo U, Galea E, Garel S, Ginhoux F, Glass CK, Gokce O, Gomez-Nicola D, González B, Gordon S, Graeber MB, Greenhalgh AD, Gressens P, Greter M, Gutmann DH, Haass C, Heneka MT, Heppner FL, Hong S, Hume DA, Jung S, Kettenmann H, Kipnis J, Koyama R, Lemke G, Lynch M, Majewska A, Malcangio M, Malm T, Mancuso R, Masuda T, Matteoli M, McColl BW, Miron VE, Molofsky AV, Monje M, Mracsko E, Nadjar A, Neher JJ, Neniskyte U, Neumann H, Noda M, Peng B, Peri F, Perry VH, Popovich PG, Pridans C, Priller J, Prinz M, Ragozzino D, Ransohoff RM, Salter MW, Schaefer A, Schafer DP, Schwartz M, Simons M, Smith CJ, Streit WJ, Tay TL, Tsai L-H, Verkhratsky A, von Bernhardi R, Wake H, Wittamer V, Wolf SA, Wu L-J, Wyss-Coray T. Microglia states and nomenclature: a field at its crossroads. Neuron. 2022;110:3458–83. https://doi.org/10.1016/j.neuron.2022.10.020.
36. Parhizkar S, Arzberger T, Brendel M, Kleinberger G, Deussing M, Focke C, Nuscher B, Xiong M, Ghasemigharagoz A, Katzmarski N, Krasemann S, Lichtenthaler SF, Müller SA, Colombo A, Monasor LS, Tahirovic S, Herms J, Willem M, Pettkus N, Butovsky O, Bartenstein P, Edbauer D, Rominger A, Ertürk A, Grathwohl SA, Neher JJ, Holtzman DM, Meyer-Luehmann M, Haass C. Loss of TREM2 function increases amyloid seeding but reduces plaque-associated ApoE. Nat Neurosci. 2019;22:191–204. https://doi.org/10.1038/s41593-018-0296-9.
37. Reed EG, Keller-Norrell PR. Minding the gap: exploring neuroinflammatory and microglial sex differences in Alzheimer's disease. Int J Mol Sci. 2023;24:17377. https://doi.org/10.3390/ijms242417377.
38. Schurz H, Salie M, Tromp G, Hoal EG, Kinnear CJ, Möller M. The X chromosome and sex-specific effects in infectious disease susceptibility. Hum Genomics. 2019;13:2. https://doi.org/10.1186/s40246-018-0185-z.
39. Ulrich JD, Ulland TK, Mahan TE, Nyström S, Nilsson KP, Song WM, Zhou Y, Reinartz M, Choi S, Jiang H, Stewart FR, Anderson E, Wang Y, Colonna M, Holtzman DM. ApoE facilitates the microglial response to amyloid plaque pathology. J Exp Med. 2018;215:1047–58. https://doi.org/10.1084/jem.20171265.
40. Villa A, Gelosa P, Castiglioni L, Cimino M, Rizzi N, Pepe G, Lolli F, Marcello E, Sironi L, Vegeto E, Maggi A. Sex-specific features of microglia from adult mice. Cell Rep. 2018;23:3501–11. https://doi.org/10.1016/j.celrep.2018.05.048.
41. Wang S, Sudan R, Peng V, Zhou Y, Du S, Yuede CM, Lei T, Hou J, Cai Z, Cella M, Nguyen K, Poliani PL, Beatty WL, Chen Y, Cao S, Lin K, Rodrigues C, Ellebedy AH, Gilfillan S, Brown GD, Holtzman DM, Brioschi S, Colonna M. TREM2 drives microglia response to amyloid-β via SYK-dependent and -independent pathways. Cell. 2022;185:4153-4169.e19. https://doi.org/10.1016/j.cell.2022.09.033.
42. Wang Y, Ulland TK, Ulrich JD, Song W, Tzaferis JA, Hole JT, Yuan P, Mahan TE, Shi Y, Gilfillan S, Cella M, Grutzendler J, DeMattos RB, Cirrito JR, Holtzman DM, Colonna M. TREM2-mediated early microglial response limits diffusion and toxicity of amyloid plaques. J Exp Med. 2016;213:667–75. https://doi.org/10.1084/jem.20151948.
43. Wlodarczyk A, Holtman IR, Krueger M, Yogev N, Bruttger J, Khorooshi R, Benmamar-Badel A, de Boer-Bergsma JJ, Martin NA, Karram K, Kramer I, Boddeke EW, Waisman A, Eggen BJ, Owens T. A novel microglial subset plays a key role in myelinogenesis in developing brain. EMBO J. 2017;36:3292–308. https://doi.org/10.15252/embj.201696056.
44. Wright AL, Zinn R, Hohensinn B, Konen LM, Beynon SB, Tan RP, Clark IA, Abdipranoto A, Vissel B. Neuroinflammation and neuronal loss precede Aβ plaque deposition in the hAPP-J20 mouse model of Alzheimer's disease. PLoS ONE. 2013;8:e59586. https://doi.org/10.1371/journal.pone.0059586.
45. Xiong J, Kang SS, Wang Z, Liu X, Kuo T-C, Korkmaz F, Padilla A, Miyashita S, Chan P, Zhang Z, Katsel P, Burgess J, Gumerova A, Ievleva K, Sant D, Yu S-P, Muradova V, Frolinger T, Lizneva D, Iqbal J, Goosens KA, Gera S, Rosen CJ, Haroutunian V, Ryu V, Yuen T, Zaidi M, Ye K. FSH blockade improves cognition in mice with Alzheimer's disease. Nature. 2022;603:470–6. https://doi.org/10.1038/s41586-022-04463-0.
46. Youmans KL, Tai LM, Kanekiyo T, Stine WB Jr, Michon SC, Nwabuisi-Heath E, Manelli AM, Fu Y, Riordan S, Eimer WA, Binder L, Bu G, Yu C, Hartley DM, Ladu MJ. Intraneuronal Abeta detection in 5xFAD mice by a new Abeta-specific antibody. Mol Neurodegener. 2012;7:8. https://doi.org/10.1186/1750-1326-7-8.
47. Yuan P, Condello C, Keene CD, Wang Y, Bird TD, Paul SM, Luo W, Colonna M, Baddeley D, Grutzendler J. TREM2 haplodeficiency in mice and humans impairs the microglia barrier function leading to decreased amyloid compaction and severe axonal dystrophy. Neuron. 2016;90:724–39. https://doi.org/10.1016/j.neuron.2016.05.003.


## Publisher's Note